

# Nondestructive Real-Time Monitoring of Enhanced Stem Cell Differentiation Using a Graphene-Au Hybrid Nanoelectrode Array

Jin-Ho Lee, Hye Kyu Choi, Letao Yang, Sy-Tsong Dean Chueng, Jeong-Woo Choi,\* and Ki-Bum Lee\*

Stem cells have attracted increasing research interest in the field of regenerative medicine because of their unique ability to differentiate into multiple cell lineages. However, controlling stem cell differentiation efficiently and improving the current destructive characterization methods for monitoring stem cell differentiation are the critical issues. To this end, multifunctional graphene–gold (Au) hybrid nanoelectrode arrays (NEAs) to: (i) investigate the effects of combinatorial physicochemical cues on stem cell differentiation, (ii) enhance stem cell differentiation efficiency through biophysical cues, and (iii) characterize stem cell differentiation in a nondestructive real-time manner are developed. Through the synergistic effects of physicochemical properties of graphene and biophysical cues from nanoarrays, the graphene-Au hybrid NEAs facilitate highly enhanced cell adhesion and spreading behaviors. In addition, by varying the dimensions of the graphene-Au hybrid NEAs, improved stem cell differentiation efficiency, resulting from the increased focal adhesion signal, is shown. Furthermore, graphene-Au hybrid NEAs are utilized to monitor osteogenic differentiation of stem cells electrochemically in a nondestructive real-time manner. Collectively, it is believed the unique multifunctional graphene-Au hybrid NEAs can significantly advance stem-cell-based biomedical applications.

Stem-cell-based regenerative medicine has attracted increasing attention in the area of biomaterial science and tissue engineering. For example, stem-cell-based approaches hold great potential in treating many musculoskeletal diseases and injuries.<sup>[1]</sup> However, the ability to differentiate stem cells into specific cell types of interest (e.g., bones, cartilages, and muscles) in a highly selective and efficient manner, and the development of nondestructive, real-time characterization methods to assay stem cell differentiation are crucial in harnessing the full potential of stem-cell-based biomaterial applications.<sup>[2,3]</sup>

Conventional methods to control stem cell differentiation using soluble cues such as growth factors, cytokines, and small organic molecules have shown limited success in achieving high differentiation specificity and efficiency. Recent findings show that biophysical (or insoluble) cues also play a critical role in guiding stem cell differentiation.<sup>[4–9]</sup> Encompassing nanotopographical and mechanical properties of microenvironment, biophysical


cues are known to be effective regulators of cytoskeletal dynamics and downstream gene expression (e.g., extracellular matrix (ECM)-integrin-cytoskeleton signaling transduction), thereby modulating stem cell behaviors such as proliferation, migration, and differentiation.<sup>[4]</sup> Therefore, there is a clear need to develop a novel method to identify the optimal biophysical cues in a combinatorial way for guiding stem cell differentiation into specific cell lineages. These identified biophysical cues can be further combined with defined soluble factors to bring synergistic differentiation conditions, which will facilitate the advancement of stem-cell-based applications such as the regeneration of certain types of damaged tissues/organs of patients.

Another critical challenge is to avoid the possible tumorigenicity associated with stem cell therapy.<sup>[3]</sup> To this end, the precise characterization of stem cell differentiation at each stage using biomarkers in a nondestructive manner while maintaining high cell viability is essential. Conventional methods for analyzing the biological characteristics of differentiated cells such as fluorescence-based methods (e.g., immunostaining

Dr. J.-H. Lee, L. Yang, S.-T. D. Chueng, Prof. K.-B. Lee  
Department of Chemistry and Chemical Biology Institute  
for Advanced Materials  
Devices and Nanotechnology (IAMDN)  
Rutgers University  
Piscataway, NJ 08854, USA  
E-mail: kblee@rutgers.edu

Dr. J.-H. Lee, H. K. Choi, Prof. J.-W. Choi  
Department of Chemical and Biomolecular Engineering  
Sogang University  
Seoul 04107, Korea  
E-mail: jwchoi@sogang.ac.kr

Prof. K.-B. Lee  
College of Pharmacy  
Kyung Hee University  
26 Kyungheedaero, Dongdaemun-gu, Seoul 02447, Korea

 The ORCID identification number(s) for the author(s) of this article can be found under <https://doi.org/10.1002/adma.201802762>.

DOI: 10.1002/adma.201802762

and fluorescence-activated cell sorting (FACS)) and analysis of the expression of biomarkers (DNAs/RNAs/proteins) (e.g., polymerase chain reaction (PCR) and Western blot) are commonly used; however, these methods typically require destructive steps such as cell fixation or cell lysis, which prevent the subsequent applications of the characterized cells.<sup>[10]</sup> Therefore, the development of novel methods that can effectively monitor stem cell differentiation dynamics in a nondestructive manner is urgent.

Addressing the challenges above, herein we demonstrate the versatility of our novel graphene-Au hybrid nanoelectrode combinatorial arrays (graphene-Au hybrid NEAs) to: (i) investigate the combinatorial effects of physicochemical cues on stem cell differentiation (Figure 1a), (ii) identify the optimal biophysical cues to enhance stem cell osteogenic differentiation (Figure 1b), and (iii) nondestructively monitor the dynamic status of stem cell differentiation in a real-time manner (Figure 1c). The osteogenesis of human mesenchymal stem cell (hMSC) was selected as a proof-of-concept model for this study.<sup>[11]</sup>

Typically, our multifunctional graphene-Au hybrid NEAs are fabricated via laser interference lithography (LIL) and physical vapor deposition (PVD) methods. We tested different variables of the graphene-Au hybrid NEAs such as pitch and pattern sizes to identify the optimal biophysical cues for osteogenic differentiation of stem cells. Reduced graphene oxide (rGO) was chemically attached and modified to the surface of Au NEAs to enhance the adhesion and spreading behaviors of

the stem cells. Since the focal adhesion and the rearrangement of the cytoskeleton is critical in determining cell behaviors, we hypothesized that our developed multifunctional graphene-Au hybrid NEAs could regulate stem cell fate through physicochemical and biophysical cues (Figure 1b).<sup>[4,12]</sup> Also, the unique physicochemical properties of rGO can promote cell adhesion and spreading behaviors on the NEAs without comprising its electrochemical property (Figure 1a).<sup>[6,13,14]</sup> Taking advantage of the high electron transfer rate based from 3D nanostructures (Figure 1c<sub>1</sub>), our graphene-Au hybrid NEAs have the potential to be utilized as an excellent electrochemical sensing platform, enabling scientists to characterize the subtle changes of biomarker expression (alkaline phosphatase (ALP, a preosteogenic marker)) (Figure 1c<sub>2</sub>). Collectively, our graphene-Au hybrid NEAs, as designed, could have the ability to enhance and monitor osteogenic differentiation of stem cell, hMSCs, in a nondestructive real-time manner.

As biophysical cues (e.g., nanotopography, elastic module, pattern dimension, and geometry) have been shown to enhance stem cell differentiation by regulating cell adhesion and spreading behaviors,<sup>[4,12,15]</sup> we generated a combinatorial graphene-Au hybrid NEA as illustrated in Figure 2a. To identify the optimized biophysical cues for stem cell osteogenesis, four different pitch sizes (400, 800, 1200, and 1600 nm) of large-scale (1 × 1 cm<sup>2</sup>) homogeneous photoresist (PR) nanohole pattern arrays were generated through the LIL technique on an indium tin oxide (ITO) substrate (Figure 2b and Figure S1, Supporting

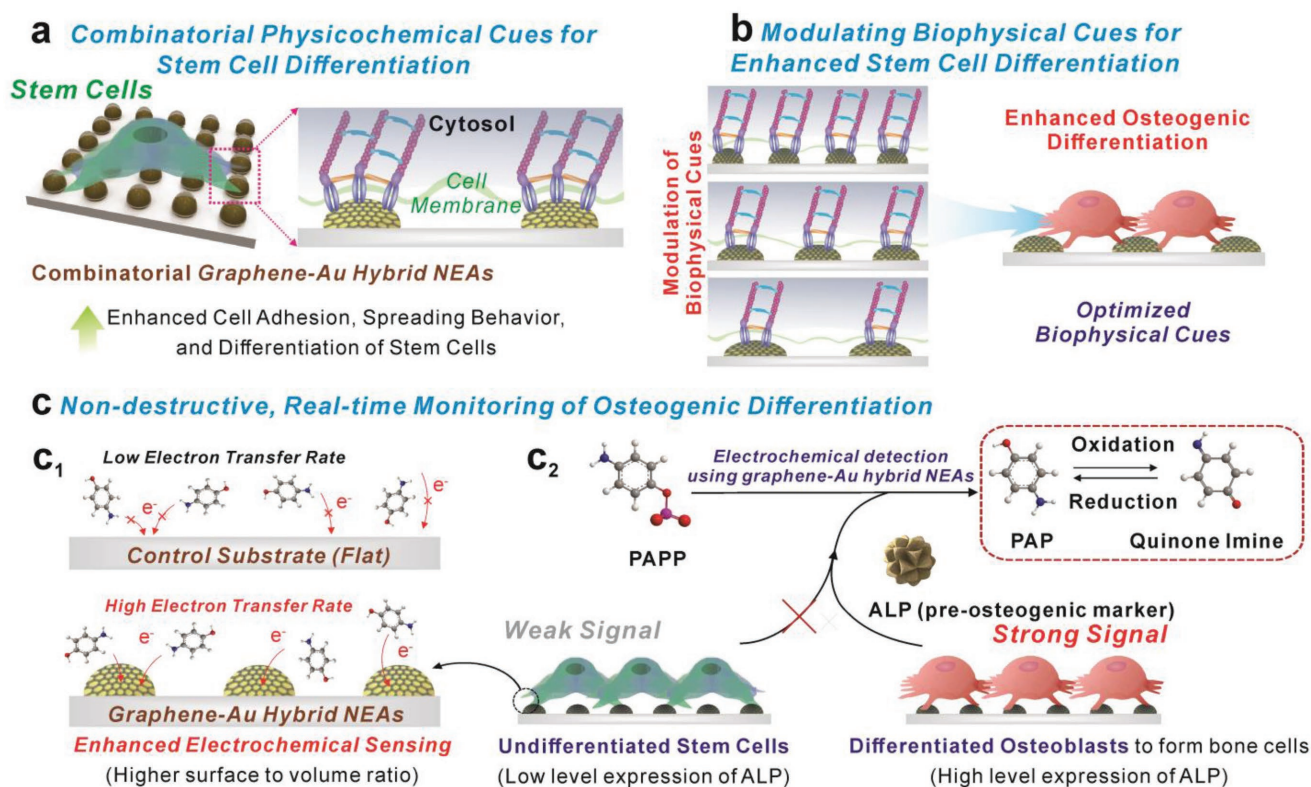


**Figure 1.** Schematic illustration of multifunctional graphene-Au hybrid nanoelectrode arrays (NEAs). a) Investigation of the combinatorial effects of physicochemical cues on stem cell. b) Identification of optimal biophysical cues for stem cell differentiation. c) Enhanced electrochemical signal for monitoring osteogenic differentiation.

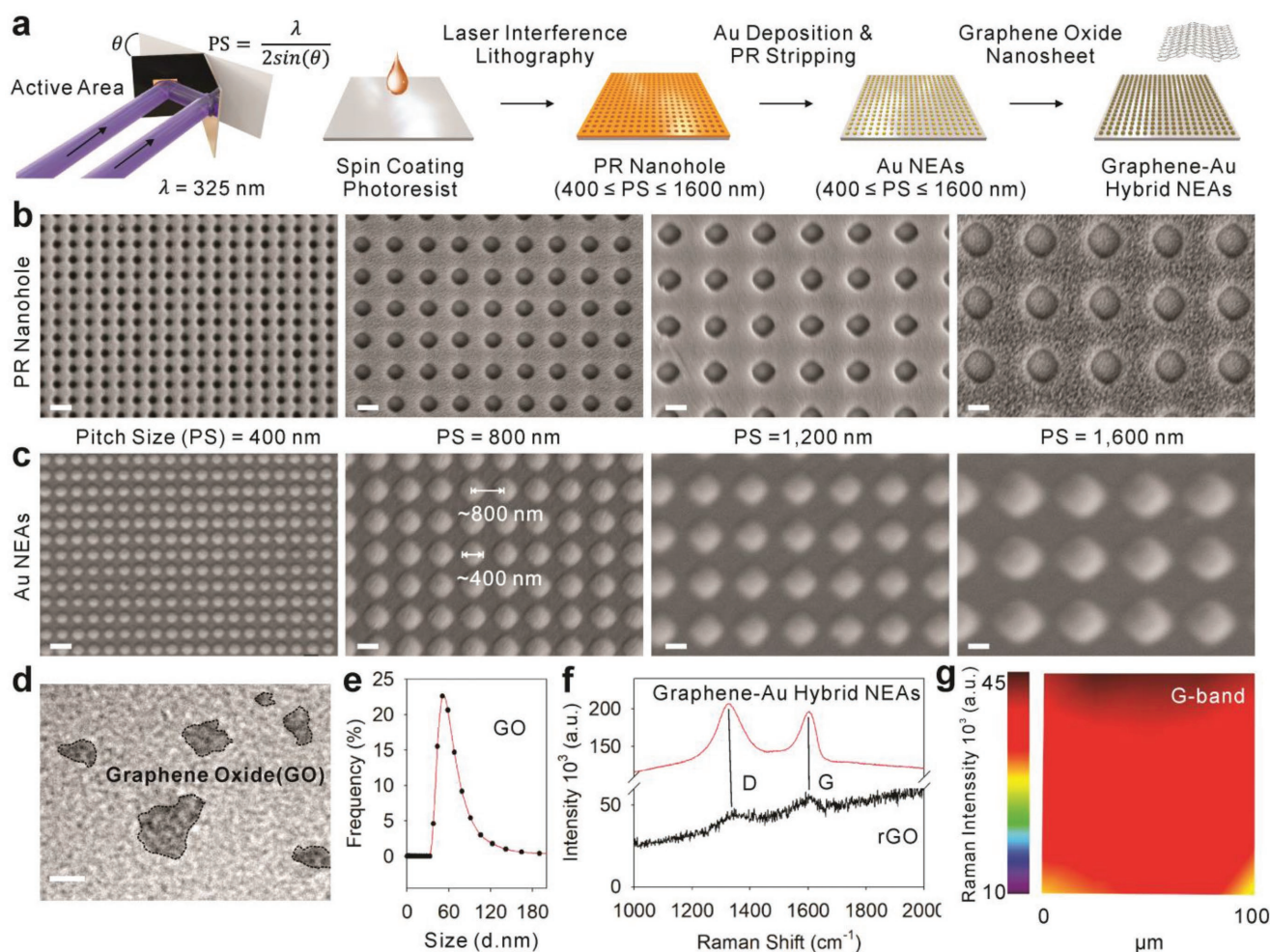


**Figure 2.** Generation of graphene-Au hybrid nanoelectrode arrays (NEAs). a) Schematic illustration of sequential steps to generate graphene-Au hybrid NEAs on ITO electrode via laser interference lithography (LIL) and metal deposition method. Representative scanning electron microscopy (SEM) images (magnification of 40 000 $\times$ ) of: b) photoresist nanohole after the LIL process and c) resulting Au NEAs after metal deposition process according to pitch size (400, 800, 1200, and 1600 nm, respectively). d) Representative transmission electron microscope (TEM) image, e) size distributions, and f) Raman spectra of synthesized graphene oxide nanosheet and after formation of graphene-Au hybrid NEAs. g) Homogeneity analysis by Raman map obtained from graphene-Au hybrid NEAs with notable Raman transitions band (G-band of graphene at around 1600  $\text{cm}^{-1}$ ). Scale bars are 500 nm (b,c) and 50 nm (d).

Information).<sup>[16]</sup> We then deposited 15 nm of chromium (Cr) as an adhesion layer and 90 nm of gold (Au) as a conducting layer via PVD onto the PR nanohole array. The PR was sequentially removed to obtain the four different sized homogenous Au NEAs with controlled width (200, 400, 600, and 800 nm), gap (200, 400, 600, and 800 nm), and height (105 nm) parameters (Figure 2c and Figure S1, Supporting Information). The pitch size and height of Au NEAs were carefully designed not only to isolate cells from the underlying flat substrate by disrupting integrin–substratum interactions but also to reconstitute integrin clustering on NEAs by controlling the width and gap of physical dimensions to the sub-micrometer range.<sup>[4,17]</sup> In parallel, graphene oxide (GO) sheets were synthesized through a modified Hummers' method with a preoxidation step. For the sufficient coating of GO onto the Au NEAs surface, the size of GO sheet was adjusted to below 200 nm by an additional filtration process to obtain smaller GO nanosheets.

To characterize the as-prepared GO sheets, transmission electron microscopy (TEM) measurement was performed (Figure 2d). We also analyzed the size distribution of GO by both dynamic light scattering (DLS) measurement and TEM images. The size distribution of the GO sheets ranged from 37.84 to 190.10 nm with an average size of  $63.75 \pm 24.63$  nm in DLS analysis (Figure 2e) and  $100.4 \pm 39.4$  nm in TEM images (Figure S2, Supporting Information). Both results clearly demonstrate the selected size distribution of GO less than 200 nm after filtration process. Further, as-prepared GO sheets were functionalized onto the surface of Au NEAs through electrostatic interactions by utilizing a chemical linker (cysteamine hydrochloride:  $\text{C}_2\text{H}_7\text{NS}$ ). Finally, GO sheets are chemically reduced by hydrazine monohydrate ( $\text{NH}_2\text{NH}_2 \cdot \text{H}_2\text{O}$ ) solution to obtain the graphene-Au hybrid NEAs. Due to the unique physicochemical structure of atomic thin layered rGO, we conducted Raman spectroscopy to properly validate the rGO

coating on the Au NEAs. As expected, Raman transition band at the location of the distinct D ( $1350\text{ cm}^{-1}$ ) and G ( $1600\text{ cm}^{-1}$ ) band of rGO were observed from both rGO (functionalized on bare Au substrate) and graphene-Au hybrid NEAs, which meets previously reports in the literature.<sup>[18]</sup> The reduction of GO to rGO on graphene-Au hybrid NEAs was also validated by the comparison of Raman intensity ratio between D and G band ( $I_D/I_G$ ) before and after the reduction process. As clearly shown in Figure S3 (Supporting Information), the  $I_D/I_G$  ratio increases from 0.90 to 1.22 as GO reduces to rGO, respectively (Figure S3, Supporting Information).<sup>[19]</sup> Moreover, a remarkably strong Raman transition band of rGO (Figure 2f) as well as intense, homogenously distributed Raman transition (distinct G band,  $1600\text{ cm}^{-1}$ , of rGO) signals over a large scan area ( $100 \times 100$  spots per  $100 \times 100\ \mu\text{m}^2$ ) (Figure 2g) were observed from the graphene-Au hybrid NEAs owing to the surface-enhanced Raman scattering effect caused by the Au nanodots.

Knowing cell adhesion/spreading behaviors and the elongated cell morphology can promote stem cell osteogenesis,<sup>[4-6,20]</sup> we hypothesized that our graphene-Au hybrid NEAs could enhance osteogenic differentiation of hMSCs through the unique physiochemical cues from our graphene-Au hybrid NEAs (Figure 3a). To test this hypothesis, hMSCs (American CryoStem), cultured on tissue culture plate (TCP), Au NEAs, and graphene-Au hybrid NEAs for 4 h, were fixed for 10 min and characterized using Hoechst to stain their nucleus and fluorescent dye (Alexa Fluor 633) to stain their cytoskeleton (F-actin). No notable difference was observed for the number of cells adhered on the TCP and Au NEAs; however, the presence of nanotopographical cues in Au NEAs allowed the cells to spread more extensively and homogeneously, compared to the experimental condition of TCP. Moreover, due to the unique physiochemical property of graphene (e.g., amphiphilic and nanoscopic properties), both the number and the size of adhered cells significantly

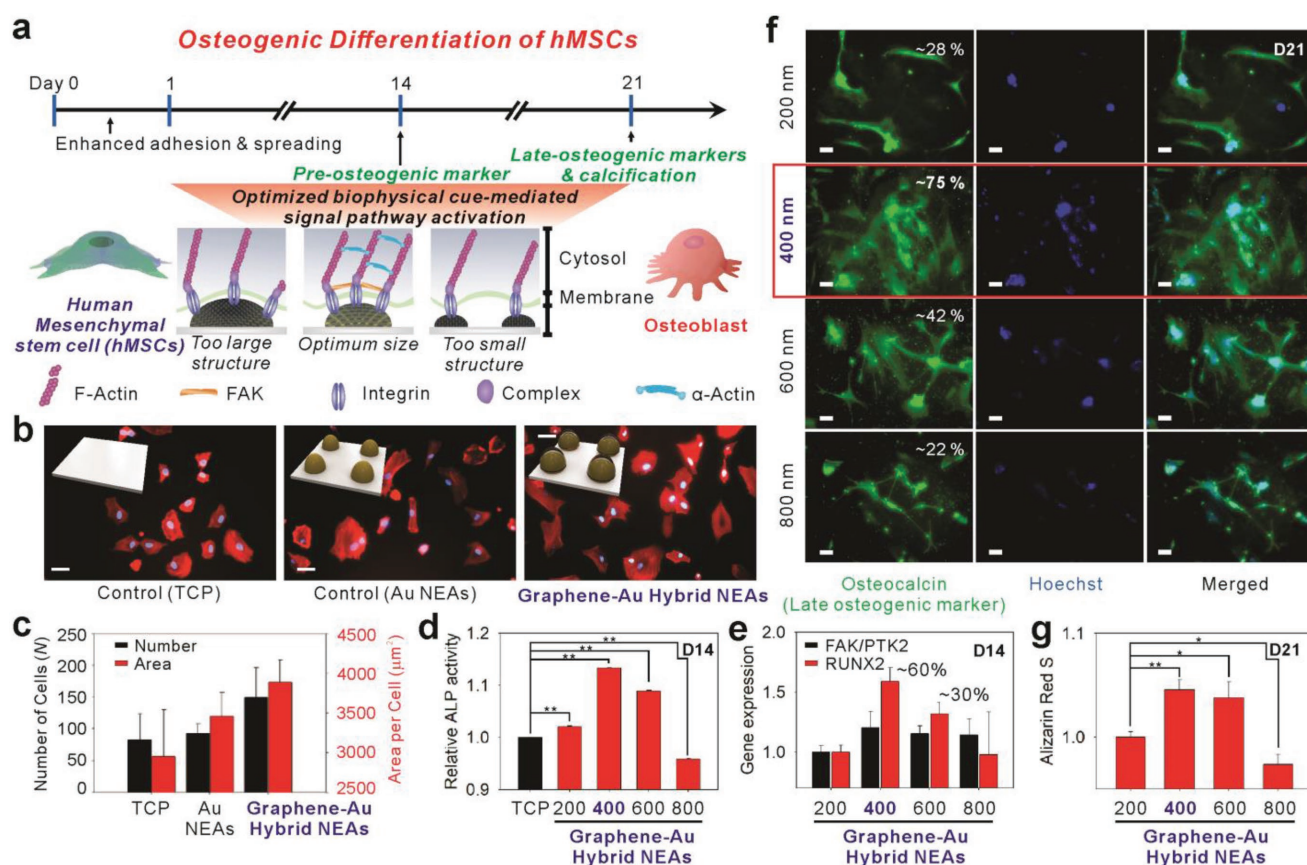


**Figure 3.** Enhanced osteogenic differentiation of hMSCs by graphene-Au hybrid NEAs. a) Schematic illustration of graphene-Au hybrid NEAs effect on the osteogenic differentiation of hMSCs. b,c) Analysis of cell adhesion and spreading behavior. b) Representative Hoechst and F-actin-stained fluorescence images of hMSCs labeled with Alexa Fluor 633 (scale bar =  $50\ \mu\text{m}$ ) and c) the calculated number of cells after washing (adhesion) and cell surface area (spreading) from F-actin-stained images of hMSCs on TCP, Au NEAs, and graphene-Au hybrid NEAs (width =  $400\text{ nm}$ ), respectively. d–g) Effect of graphene-Au hybrid NEAs on osteogenic differentiation of hMSCs based on different width size range from  $200$  to  $800\text{ nm}$ . d) Alkaline phosphatase (ALP) assay to confirm the expression of the preosteogenic marker based on different pitch size. e) PCR analysis of osteogenic markers including runt-related transcription factor 2 (RUNX2) and focal adhesion kinase (FAK) for verifying a nanotopographic effect. f) Fluorescence images of hMSCs differentiated into osteoblasts stained for osteocalcin with Alexa 594 (red, left column), a nucleus with Hoechst (blue, middle column), and merged (right column) (scale bar =  $50\ \mu\text{m}$ ). g) Quantitative analysis of calcium expression by extracting Alizarin red S based on different width size. Results are average of absorbance signals ( $405$  and  $562\text{ nm}$  for ALP and Alizarin red S, respectively, obtained from three independent experiments). (The error bars represent mean  $\pm$  s.d.;  $n = 3$ ,  $*p < 0.05$ ,  $**p < 0.001$  by one-way ANOVA with Tukey post hoc test.)

increased on the graphene-Au hybrid NEAs, compared to that of TCP and Au NEA conditions (Figure 3b). We quantitatively analyzed the number and the size of adhered cells using five  $1320 \times 1320 \mu\text{m}^2$  area-fluorescent images, randomly selected from each condition. The average number of cells were  $83.0 \pm 40.3$ ,  $92.6 \pm 15.2$ , and  $149.4 \pm 46.7$ , and the average size of the cells were  $2955.9 \pm 584.9$ ,  $3457.9 \pm 298.9$ , and  $3890.8 \pm 272.6 \mu\text{m}^2$ , corresponding to the TCP, Au NEA, and graphene-Au hybrid NEA conditions, respectively (Figure 3c).

To examine further, hMSCs that were grown on graphene-Au hybrid NEAs for a day were treated with differentiation induction medium (osteogenic medium: OM) to study the optimal biophysical cues on osteogenesis. All the cells treated with OM showed the expression of ALP (preosteogenic marker) regardless of substrate types used; however, hMSCs on the graphene-Au hybrid NEAs with 400 nm sized (in diameter) nanodots among the four different conditions (pattern sizes: 200, 400, 600, and 800 nm) (Figure 3d) showed the highest ALP activity on day 14 (D14), supporting the synergistic effect of the biophysical cues combined with the soluble cues (Figure 3d).<sup>[21]</sup> We also conducted real-time quantitative PCR on D14 to detect biomarkers of osteoblast lineage such as runt-related transcription factor 2 (RUNX2) and focal adhesion kinase/protein tyrosine kinase 2 (FAK/PTK2) genes to investigate the effects of each nanopattern on osteogenic differentiation.<sup>[9]</sup> It is known that appropriate biophysical cues, such as nanotopography and pattern dimension, can enhance the formation of integrin-mediated small clustering adhesion sites termed focal adhesions (FAs),<sup>[4]</sup> which affect cell spreading behavior and facilitate lamellipodial protrusions.<sup>[22]</sup> Moreover, the formation of FA complexes stimulates multiple intracellular signaling cascades such as the mitogen-activated protein kinase-extracellular signal-regulated kinase (MAPK-ERK) 1/2 pathway that activates RUNX2, resulting in increased osteogenic differentiation.<sup>[23]</sup> We also confirmed the clear co-related upregulation between the FAK/PTK2 gene and the RUNX2 gene in our tested graphene-Au hybrid NEAs. In particular, as predicted from the ALP activity assay, the level of molecular markers for both osteoblast lineage (RUNX2) and the focal adhesion kinase (FAK/PTK2) gene also showed the highest expression from the 400 nm sized graphene-Au hybrid NEA condition (Figure 3e). This indicates that early osteogenic differentiation can be synergistically enhanced through the proper choice of biophysical cues. Immunostaining also showed the highest coverage and expression of osteocalcin from the 400 nm diameter graphene-Au hybrid NEA condition (Figure 3f).<sup>[8,9,21]</sup> From the Alizarin red S assay, which checks the level of calcification, one of the most significant indicators for bone regeneration, we also observed cells grown on the 400 nm sized graphene-Au hybrid NEAs showed the highest level of calcification (Figure 3g).<sup>[8]</sup> Collectively, the above results support our hypothesis that appropriate biophysical cues of our graphene-Au hybrid NEAs can enhance the formation of mature osteoblasts, which is highly desirable for further in vivo applications such as treating bone defects.

Furthermore, we developed our graphene-Au hybrid NEAs (400 nm sized graphene-Au hybrid NEAs, hereafter termed graphene-Au hybrid NEAs) as a nondestructive real-time electrochemical sensing platform to monitor stem cell differentiation

(Figure 4). Since most of the electrochemical reaction happens in proximity to the electrode surface, the surface dimension and its modification are crucial for the performance of electrochemical sensing. For this purpose, nanomaterial (Au and carbon)-based electrochemical sensors have been developed owing to their unique physicochemical properties including high conductivity, inertness, and biocompatibility.<sup>[13,14,24]</sup> Additionally, the higher surface-to-volume ratio of the nanostructures can also increase the electrochemical sensing performance.<sup>[14,25]</sup> We conducted cyclic voltammograms (CV) by using  $1 \times 10^{-3} \text{ M}$  of ferrocyanide  $[\text{Fe}(\text{CN})_6]^{4-}$  as a well-defined electroactive (reduction and oxidation: redox) chemical in phosphate buffered saline (PBS, pH 7.4) at a scan rate of  $50 \text{ mV s}^{-1}$  to measure the electrochemical signal from each electrode (bare ITO, Au NEAs, and graphene-Au hybrid NEAs) (Figure 4b). As expected, there was no observable faradaic current on the bare ITO substrate. However, a large current, intense oxidation and reduction peak ( $I_{\text{PA}}$  and  $I_{\text{PC}}$ ) were observed on both the rGO-ITO and Au NEAs. In particular, graphene-Au hybrid NEAs displayed a narrower and higher  $I_{\text{PA}}$  and  $I_{\text{PC}}$  due to the better electron transfer rate and faster diffusion of oxidant/reductant obtained through the additive effect obtained by both rGO and Au NEAs.<sup>[13,14]</sup> We also validated the electrochemical performance based on the reduction degree of rGO. As shown in Figure S4 (Supporting Information), no observable faradaic current on the GO-coated ITO substrate, which could be due to the impeded electron transfer. However, an intense  $I_{\text{PA}}$  and  $I_{\text{PC}}$  were observed after reduction process. The signal was kept increased and saturated after 9 h reduction.<sup>[26]</sup>

We then utilized our graphene-Au hybrid NEAs to examine an ALP-based enzymatic reaction in a cell-free configuration as an initial proof-of-concept before monitoring the osteogenic differentiation process of hMSCs. The expression of ALP, a major biomarker for osteogenesis,<sup>[27]</sup> arose sequentially during the osteogenic differentiation. As shown in Figure 4a, ALP catalytically hydrolyzed the P-aminophenyl phosphate (PAPP) to produce electroactive *p*-aminophenol (PAP), and the redox reaction between PAP and quinone imine (QI) was monitored through cyclic voltammogram by utilizing graphene-Au hybrid NEAs as a sensing platform (Figure 4a). Before the addition of ALP, no observable redox peak was monitored for the PAPP ( $1 \times 10^{-3} \text{ M}$ ) dissolved PBS solution. However, observable redox peaks were obtained 30 min after the addition of ALP into the solution, at  $\approx 0.2 \text{ V}$  for the oxidation ( $I_{\text{PA}}$ ) potential and  $0.01 \text{ V}$  for the reduction ( $I_{\text{PC}}$ ) potential (Figure 4c). Comparably, no observable oxidation signal ( $I_{\text{PA}}$ ) was obtained on the bare ITO substrate for neither condition: absence or presence of ALP. Particularly, a remarkable oxidation peak was observed only at the graphene-Au hybrid NEAs when ALP was presented, which proved its excellent sensitivity for the electrochemical detection of PAP resulted from ALP catalytic reaction (Figure 4d). To support these results, we also calculated the highest energy occupied molecular orbital (HOMO) and lowest energy unoccupied molecular orbital (LUMO) of PAP molecule and compare it to the band edge positions of rGO, Au, and ITO that are reported in literature.<sup>[28]</sup> When no voltage bias is applied, rGO has less barrier to receive electron from PAP molecules, which leads to the oxidation of PAP into QI (Figure S5, Supporting Information). In addition, graphene-Au hybrid NEAs with increased

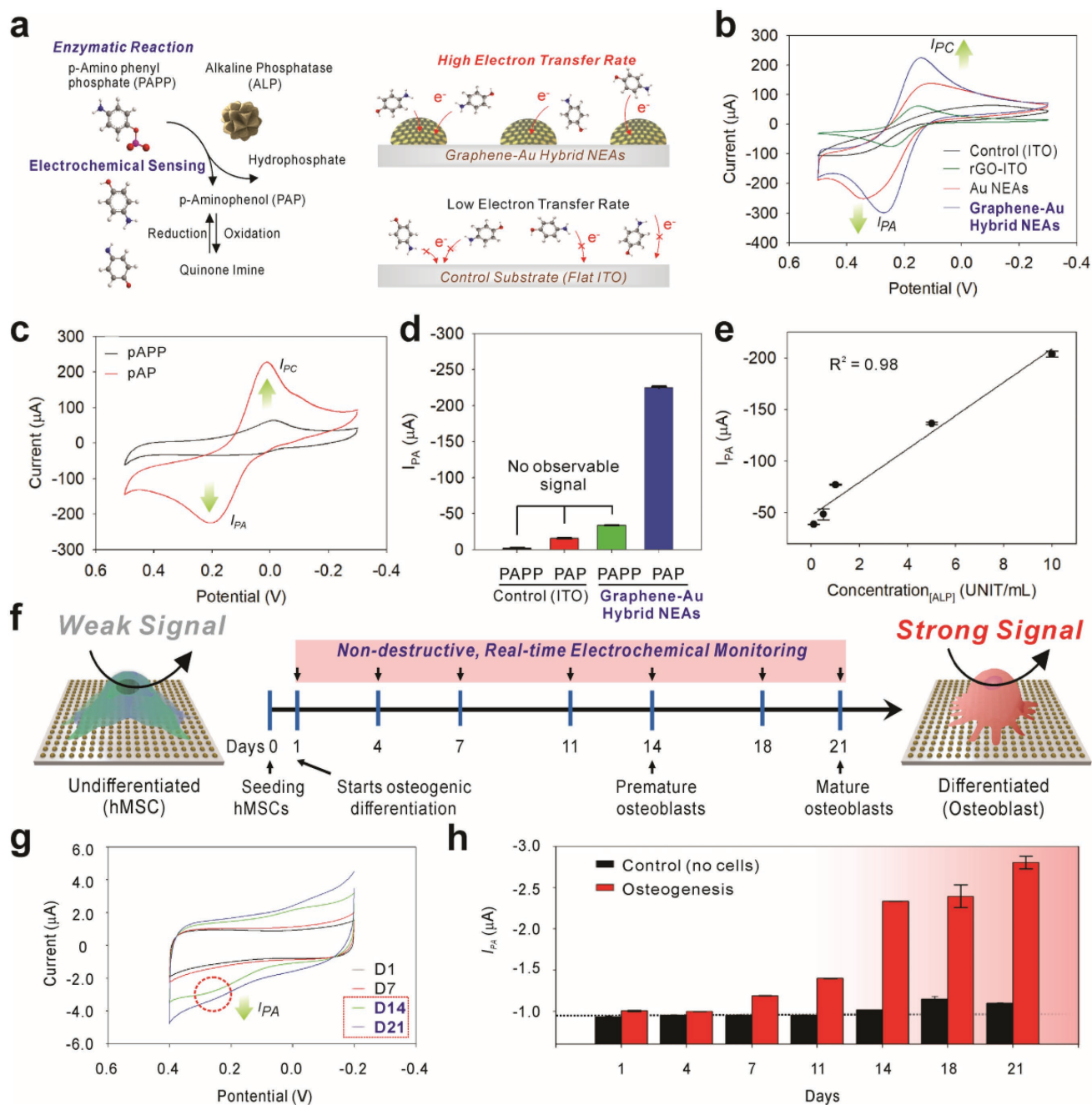


**Figure 4.** Utilization of graphene-Au hybrid NEAs as an electrochemical sensing platform for in situ monitoring of osteogenic differentiation of hMSCs. a) Schematic illustration of an enzymatic reaction and electrochemical sensing mechanism of alkaline phosphatase (ALP) and improved electron transfer kinetic based on the 3D surface in graphene hybrid NEAs compared to 2D flat ITO surface. b) Cyclic voltammogram of  $1 \times 10^{-3}$  M of  $[\text{Fe}(\text{CN})_6]^{4-}$  dissolved in DPBS obtained at a  $50 \text{ mV s}^{-1}$  scan rate using a bare ITO substrate, rGO-coated ITO substrate, Au NEAs, and graphene-Au NEAs, respectively. c) Cyclic voltammogram of P-aminophenyl phosphate (PAPP) on graphene-Au NEAs before and after enzyme reaction with alkaline phosphatase (ALP). d) Anodic peak (oxidation potential:  $I_{PA}$ ) value change achieved from cyclic voltammogram of PAPP, before and after enzyme reaction (ALP), on bare ITO substrate and graphene-Au hybrid NEAs. e) The linear correlations between concentrations of ALP and the current signal at oxidation potential ( $I_{PA}$ ) of cyclic voltammetry. f) Schematic illustration of electrochemical signal change between undifferentiated and differentiated (osteocyte) hMSCs based on ALP generation. g) Cyclic voltammogram, and h) calculated  $I_{pc}$  values from time-dependent monitoring (range from D1 to D21) of hMSCs during osteogenic differentiation.  $8.0 \times 10^3$  cells are seeded on  $0.4 \text{ cm}^2$  area and treated with osteogenic differentiation medium (OM). The medium was changed after each electrochemical measurement.

electrode surface area could also increase electron transfer rate by facilitating the electron and mass diffusion. Such improvements can be directly supported by the increased  $I_{PA}$  shown

in Figure 4c and narrowed voltage difference between  $I_{PA}$  and  $I_{PC}$  shown in Figure 4b. Moreover, graphene-Au hybrid NEAs showed good linearity ( $R^2 = 0.98$ ) at different concentrations

(range from 0.1 to 10 units mL<sup>-1</sup>) of ALP with a limit of detection (LOD) of 0.03 unit mL<sup>-1</sup> (Figure 4e) which well agreed with previously reported quantitative ALP assays.<sup>[29]</sup> Additionally, the clear oxidation peak was observed within 10 min after addition of ALP, and the overall enzyme reaction was starting to saturate at ≈40 min (Figure S6, Supporting Information).

After verifying the electrochemical property of graphene-Au hybrid NEAs in cell-free condition, hMSCs (2.0 × 10<sup>4</sup> cells cm<sup>-2</sup>) that were grown on graphene-Au hybrid NEAs for a day were treated with OM. The cyclic voltammetry was conducted for differentiation period (three weeks) with the addition of PAPP molecule (Figure S7, Supporting Information) for real-time monitoring of the osteogenic differentiation of hMSCs in a nondestructive manner (Figure 4f). We observed no obvious redox peaks on the voltammogram up to D7 even though the background signal is slightly increased. In contrast, clear, distinct redox peaks were observed in the period of the premature (D14) and mature (D21) osteoblast formation. The calculated *I*<sub>PA</sub> values from time-dependent monitoring (range from D1 to D21) of hMSCs during osteogenic differentiation demonstrated the sequential increment of ALP activity as expected (Figure S8, Supporting Information). In particular, the remarkable signal increment was observed from D14, where premature osteoblast starts to form (Figure 4g). Additionally, graphene-Au hybrid NEAs also showed excellent stability by maintaining the *I*<sub>PA</sub> value for three weeks under the cell-free condition (Figure 4h).

We also analyzed for myogenic differentiation electrochemically at D21 (Figure S9, Supporting Information) to show that our graphene-Au hybrid NEAs could discriminate osteogenic differentiation from other types of differentiation. Compared to hMSCs, myoblast cell also demonstrated higher ALP activity;<sup>[30]</sup> however, osteoblasts expressed ≈2 times higher signals ( $\Delta I_{PA} = -1.80 \mu A$ ) relative to myoblasts ( $\Delta I_{PA} = -0.82 \mu A$ ) which showed the ability of graphene-Au hybrid NEAs to discriminate osteogenic differentiation from other differentiation. Supportably, cell-destructive PNPP-based optical ALP assay also demonstrated similar trends on ALP activity of each cell line (undifferentiated hMSC, osteoblast, and myoblast) observed by graphene-Au hybrid NEAs. Thus, we believe that our graphene-Au hybrid NEAs will be particularly valuable for enhancing and monitoring stem cell behaviors through unique biophysical and electrochemical properties. The nondestructive, real-time monitoring of stem cell differentiation would be valuable for the clinical application of stem cell therapies to repair the damaged tissue/organs of patients.

In summary, we have successfully developed multifunctional graphene-Au hybrid NEAs for modulating the extent of osteogenic differentiation of stem cells. Potentially, our developed approach can be beneficial for deconvoluting biophysical cues from the complex microenvironmental cues and identify the combinatorial cues to enhance stem cell differentiation. More detailed mechanistic studies on how the combination of physicochemical and biophysical cues modulate the signaling cascades involved in stem cell osteogenesis are currently under investigation. Furthermore, due to the excellent biocompatibility and electrochemical performance of our hybrid NEAs, the osteogenic differentiation of hMSCs was successfully monitored in both nondestructive and real-time manner. Since the destructive analysis process such as cell lysis and

cell fixation are not necessary for assaying the osteogenic differentiation of hMSCs for transplantation, our developed combinatorial arrays and novel electrochemical detection method can bring a breakthrough in the preclinical investigation of differentiated osteoblasts. Collectively, this work will not only advance stem cell differentiation assays by providing a practical, nondestructive, real-time monitoring tool but also help scientists understand the fundamental interactions between nanostructures and stem cells better.

## Supporting Information

Supporting Information is available from the Wiley Online Library or from the author.

## Acknowledgements

K.B.L. acknowledges the partial financial support from the NIH R21 (1R21AR071101-01), the NSF (CHE-1429062), and New Jersey Commission on Spinal Cord (CSCR16ERG019). J.W.C. acknowledges partial financial support from the NRF (2013K1A4A3055268) and (2016R1A6A1A03012845) funded by MSIP and the ME of Korea. The authors are also grateful to Thanapat Pongkulapa and Dr. Tae-Hyung Kim for their kind support and valuable discussion.

## Conflict of Interest

The authors declare no conflict of interest.

## Keywords

biosensing, graphene-Au hybrid nanoelectrode arrays, nondestructive real-time detection, osteogenesis from stem cells, stem cell differentiation

Received: April 30, 2018

Revised: June 16, 2018

Published online:

- [1] a) C. E. Muller-Sieburg, H. B. Sieburg, J. M. Bernitz, G. Cattarossi, *Blood* **2012**, *119*, 3900; b) P. Cahan, G. Q. Daley, *Nat. Rev. Mol. Cell Biol.* **2013**, *14*, 357; c) P. S. Knoepfler, *Adv. Drug Delivery Rev.* **2015**, *82*, 192; d) J. L. Sternecker, P. Reinhardt, H. R. Scholer, *Nat. Rev. Genet.* **2014**, *15*, 625.
- [2] a) K. H. Narsinh, N. Sun, V. Sanchez-Freire, A. S. Lee, P. Almeida, S. Hu, T. Jan, K. D. Wilson, D. Leong, J. Rosenberg, M. Yao, R. C. Robbins, J. C. Wu, *J. Clin. Invest.* **2011**, *121*, 1217; b) U. Ben-David, N. Benvenisty, *Nat. Rev. Cancer* **2011**, *11*, 268.
- [3] a) A. S. Lee, C. Tang, M. S. Rao, I. L. Weissman, J. C. Wu, *Nat. Med.* **2013**, *19*, 998; b) P. S. Knoepfler, *Stem Cells* **2009**, *27*, 1050.
- [4] M. J. Dalby, N. Gadegaard, R. O. Oreffo, *Nat. Mater.* **2014**, *13*, 558.
- [5] a) K. A. Kilian, B. Bugarija, B. T. Lahn, M. Mrksich, *Proc. Natl. Acad. Sci. USA* **2010**, *107*, 4872; b) X. Wang, S. Li, C. Yan, P. Liu, J. Ding, *Nano Lett.* **2015**, *15*, 1457.
- [6] W. C. Lee, C. H. Lim, H. Shi, L. A. Tang, Y. Wang, C. T. Lim, K. P. Loh, *ACS Nano* **2011**, *5*, 7334.
- [7] a) R. McBeath, D. M. Pirone, C. M. Nelson, K. Bhadriraju, C. S. Chen, *Dev. Cell* **2004**, *6*, 483; b) J. H. Tsui, K. Janebodin,

- N. Ieronimakis, D. M. P. Yama, H. S. Yang, R. Chavanachat, A. L. Hays, H. Lee, M. Reyes, D. H. Kim, *ACS Nano* **2017**, *11*, 11954.
- [8] T. R. Nayak, H. Andersen, V. S. Makam, C. Khaw, S. Bae, X. Xu, P. L. Ee, J. H. Ahn, B. H. Hong, G. Pastorin, B. Ozyilmaz, *ACS Nano* **2011**, *5*, 4670.
- [9] J. Yang, L. E. McNamara, N. Gadegaard, E. V. Alakpa, K. V. Burgess, R. M. Meek, M. J. Dalby, *ACS Nano* **2014**, *8*, 9941.
- [10] a) H. S. Goodwin, A. R. Bicknese, S. N. Chien, B. D. Bogucki, C. O. Quinn, D. A. Wall, *Biol. Blood Marrow Transplant.* **2001**, *7*, 581; b) T. H. Kim, C. H. Yea, S. T. Chueng, P. T. Yin, B. Conley, K. Dardir, Y. Pak, G. Y. Jung, J. W. Choi, K. B. Lee, *Adv. Mater.* **2015**, *27*, 6356.
- [11] a) M. F. Pittenger, A. M. Mackay, S. C. Beck, R. K. Jaiswal, R. Douglas, J. D. Mosca, M. A. Moorman, D. W. Simonetti, S. Craig, D. R. Marshak, *Science* **1999**, *284*, 143; b) P. M. Tsimbouri, P. G. Childs, G. D. Pemberton, J. Yang, V. Jayawarna, W. Orapiriyakul, K. Burgess, C. González-García, G. Blackburn, D. Thomas, C. Vallejo-Giraldo, M. J. P. Biggs, A. S. G. Curtis, M. Salmerón-Sánchez, S. Reid, M. J. Dalby, *Nat. Biomed. Eng.* **2017**, *1*, 758; c) J. M. Kanczler, R. O. Oreffo, *Eur. Cells Mater.* **2008**, *15*, 100.
- [12] a) M. P. Lutolf, P. M. Gilbert, H. M. Blau, *Nature* **2009**, *462*, 433; b) W. Chen, Y. Shao, X. Li, G. Zhao, J. Fu, *Nano Today* **2014**, *9*, 759; c) T. Iskratsch, H. Wolfenson, M. P. Sheetz, *Nat. Rev. Mol. Cell Biol.* **2014**, *15*, 825; d) W. L. Murphy, T. C. McDevitt, A. J. Engler, *Nat. Mater.* **2014**, *13*, 547.
- [13] a) D. Chen, H. Feng, J. Li, *Chem. Rev.* **2012**, *112*, 6027; b) M. Zhou, Y. Zhai, S. Dong, *Anal. Chem.* **2009**, *81*, 5603.
- [14] J. H. Lee, B. K. Oh, J. W. Choi, *Biosens. Bioelectron.* **2013**, *49*, 531.
- [15] A. J. Engler, S. Sen, H. L. Sweeney, D. E. Discher, *Cell* **2006**, *126*, 677.
- [16] K. S. Kim, H. Jeong, M. S. Jeong, G. Y. Jung, *Adv. Funct. Mater.* **2010**, *20*, 3055.
- [17] C. Selhuber-Unkel, M. Lopez-Garcia, H. Kessler, J. P. Spatz, *Biophys. J.* **2008**, *95*, 5424.
- [18] a) T. H. Kim, S. Shah, L. Yang, P. T. Yin, M. K. Hossain, B. Conley, J. W. Choi, K. B. Lee, *ACS Nano* **2015**, *9*, 3780; b) X. Li, W. C. H. Choy, X. Ren, D. Zhang, H. Lu, *Adv. Funct. Mater.* **2014**, *24*, 3114; c) N. Yi, C. Zhang, Q. Song, S. Xiao, *Sci. Rep.* **2016**, *6*, 25134.
- [19] a) S. Stankovich, D. A. Dikin, R. D. Piner, K. A. Kohlhaas, A. Kleinhammes, Y. Jia, Y. Wu, S. T. Nguyen, R. S. Ruoff, *Carbon* **2007**, *45*, 1558; b) S. Eigler, C. Dotzer, A. Hirsch, *Carbon* **2012**, *50*, 3666.
- [20] M. H. You, M. K. Kwak, D. H. Kim, K. Kim, A. Levchenko, D. Y. Kim, K. Y. Suh, *Biomacromolecules* **2010**, *11*, 1856.
- [21] S. Khetan, M. Guvendiren, W. R. Legant, D. M. Cohen, C. S. Chen, J. A. Burdick, *Nat. Mater.* **2013**, *12*, 458.
- [22] B. Geiger, A. Bershadsky, *Curr. Opin. Cell Biol.* **2001**, *13*, 584.
- [23] a) Q. Chen, P. Shou, C. Zheng, M. Jjiang, G. Cao, Q. Yang, J. Cao, N. Xie, T. Velletri, X. Zhang, C. Xu, L. Zhang, H. Yang, J. Hou, Y. Wang, Y. Shi, *Cell Death Differ.* **2016**, *23*, 1128; b) C. Ge, Q. Yang, G. Zhao, H. Yu, K. L. Kirkwood, R. T. Franceschi, *J. Bone Miner. Res.* **2012**, *27*, 538.
- [24] a) J. Wang, *Electroanalysis* **2005**, *17*, 7; b) A. M. Yu, Z. J. Liang, J. Cho, F. Caruso, *Nano Lett.* **2003**, *3*, 1203.
- [25] a) Y. S. Fu, S. H. Ji, X. Chen, X. C. Ma, R. Wu, C. C. Wang, W. H. Duan, X. H. Qiu, B. Sun, P. Zhang, J. F. Jia, Q. K. Xue, *Phys. Rev. Lett.* **2007**, *99*, 256601; b) C. Zhu, G. Yang, H. Li, D. Du, Y. Lin, *Anal. Chem.* **2015**, *87*, 230.
- [26] A. Ambrosi, C. K. Chua, A. Bonanni, M. Pumera, *Chem. Rev.* **2014**, *114*, 7150.
- [27] a) J. N. Beresford, J. H. Bennett, C. Devlin, P. S. Leboy, M. E. Owen, *J. Cell Sci.* **1992**, *102*, 341; b) G. R. Beck, E. C. Sullivan, E. Moran, B. Zerler, *J. Cell Biochem.* **1998**, *68*, 269.
- [28] a) N. Balis, E. Stratakis, E. Kymakis, *Mater. Today* **2016**, *19*, 580; b) J.-S. Yeo, R. Kang, S. Lee, Y.-J. Jeon, N. Myoung, C.-L. Lee, D.-Y. Kim, J.-M. Yun, Y.-H. Seo, S.-S. Kim, *Nano Energy* **2015**, *12*, 96.
- [29] H. Jiao, J. Chen, W. Li, F. Wang, H. Zhou, Y. Li, C. Yu, *ACS Appl. Mater. Interfaces* **2014**, *6*, 1979.
- [30] a) A. Safadi, E. Livne, M. Silbermann, A. Z. Reznick, *J. Histochem. Cytochem.* **1991**, *39*, 199; b) A. Dellavalle, M. Sampaolesi, R. Tonlorenzi, E. Tagliafico, B. Sacchetti, L. Perani, A. Innocenzi, B. G. Galvez, G. Messina, R. Morosetti, S. Li, M. Belicchi, G. Peretti, J. S. Chamberlain, W. E. Wright, Y. Torrente, S. Ferrari, P. Bianco, G. Cossu, *Nat. Cell Biol.* **2007**, *9*, 255.